

NUMERICAL ANALYSIS AND SCIENTIFIC COMPUTING
PREPRINT SERIA

**Numerical simulation of surface
acoustic wave actuated enantiomer
separation by the finite element
immersed boundary method**

K. BELEKE-MAXWELL T. FRANKE R.H.W. HOPPE
C. LINSENMANN

PREPRINT #29



DEPARTMENT OF MATHEMATICS
UNIVERSITY OF HOUSTON

AUGUST 2014

NUMERICAL SIMULATION OF SURFACE ACOUSTIC WAVE ACTUATED ENANTIOMER SEPARATION BY THE FINITE ELEMENT IMMERSSED BOUNDARY METHOD

K. BELEKE-MAXWELL*, T. FRANKE†, R.H.W. HOPPE‡, AND C. LINSNMANN§

Abstract. Enantiomers are chiral objects such as chemical molecules that can be distinguished by their handedness. They typically occur as racemic compounds of left- and right-handed species which may have completely different properties. Therefore, in applications such as drug design in pharmacology, enantiomer separation is an important issue. Here, we present a new technology for enantiomer separation by surface acoustic wave generated vorticity patterns consisting of pairwise counter-rotating vortices in a carrier fluid. The enantiomers are injected onto the surface of the fluid between two counter-rotating vortices such that right-handed (left-handed) enantiomers get attracted by left-rotating (right-rotating) vortices. In particular, we are concerned with the numerical simulation of this separation process by an application of the finite element immersed boundary method which relies on the solution of a coupled system consisting of the incompressible Navier-Stokes equations and the equations of motion of the immersed enantiomers described with respect to an Eulerian and a Lagrangian coordinate system. For a model system of deformable, initially L-shaped enantiomers the results of the numerical simulations reveal a perfect separation.

Key words. enantiomer separation, surface acoustic waves, finite element immersed boundary method

AMS subject classifications. 65M60, 74L15, 76Z05, 92C10, 92C50

1. Introduction. A geometric object is said to be chiral, if it is not identical to its mirror image, and achiral, otherwise. A chiral object and its mirror image are called enantiomers (or optical isomers). Since the word chiral stems from the Greek $\chi\epsilon\iota\rho$ which means 'hand', one distinguishes enantiomers by their handedness (right- resp. left-handedness, or R- resp. L-form, or (+)- resp. (−)-form). In chemistry, chirality refers to a molecule that is not superposable on its mirror image (cf. Figure 1.1). Compounds consisting of molecules of the same handedness are called single-enantiomeric, enantiopure, or unichiral, whereas compounds consisting of the same amount of R- and L-form enantiomers are referred to as racemic. The discovery of molecular chirality goes back to the nineteenth century when in 1815 the French physicist J.-B. Biot [3] studied organic compounds and found that some of them rotate polarized light in the noncrystalline state, i.e., in the liquid or solvent state. Biot was aware that the optical rotation is due to structural properties of the molecules, and he referred to them as 'substances moléculairement actives'. Three decades later, in 1848 the French chemist and microbiologist Louis Pasteur [27] (see also [15]) discovered hemihedrism in crystals of dextro-tartaric acid ((+)-tartaric acid), i.e., the existence of small facets at alternate corners of the crystals that make the crystals dissymmetric (i.e., chiral). Pasteur [28] also examined racemic acid, earlier discovered by

*Center for Research in Scientific Computation, North Carolina State University, Raleigh, NC 27695-8212, USA The author has been supported by the NSF grant DMS-1115658.

†Institute of Physics, University of Augsburg, D-86159 Augsburg, Germany. The author has been supported by the DFG Priority Programs SPP 1253 and SPP 1506.

‡Institute of Mathematics, University of Augsburg, D-86159, Augsburg, Germany, and Department of Mathematics, University of Houston, Houston, TX 77204-3008, USA (rohop@math.uh.edu). The author has been supported by the DFG Priority Programs SPP 1253 and SPP 1506, by the NSF grants DMS-0914788, DMS-1115658, and by the European Science Foundation within the Networking Programme 'OPTPDE'.

§Institute of Mathematics, University of Augsburg, D-86159, Augsburg, Germany. The author has been supported by the DFG Priority Program SPP 1253.

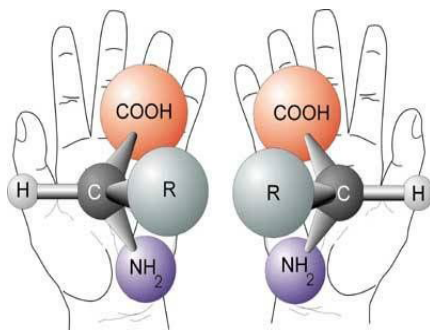


FIG. 1.1. *Left- and right-handed enantiomer*

Gay-Lussac in 1826 which does not rotate polarized light and is chemically inactive, and found that there are two different crystals with hemihedral facets inclined to the right and to the left. Pasteur managed to separate the two kind of crystals ((+)- and (-)-tartaric acid) and found that in solvent state they rotate polarized light with the rotations being equal in magnitude but opposite in direction. In 1858, Pasteur also discovered enantiomer selectivity when he studied solutions of racemic acid enriched by microorganisms and found that the (+)-enantiomers were more rapidly metabolized than the (-)-enantiomers concluding that this process must be due to a selective interaction of enantiomers with key chiral molecules within the microorganisms. Roughly twenty years after Pasteur's fundamental work, the Dutch and French chemists J.H. van 't Hoff [17] and J.A. LeBel [24] independently discovered the tetrahedral carbon atom as a basis for molecular chirality and thus paved the way for the elucidation of the structures of organic compounds.

During the first half of the last century, several attempts have been made to derive appropriate models for chiral molecules based on electronic theories explaining their optical activity. Among them are Born's theory of coupled oscillators [6] and the quantum mechanical one-electron theory due to Condon et al. [10] which - opposed to Born's assumption - proves that a single electron can be optically active under the influence of a chiral potential. However, the quantum mechanical description of chirality leads to a contradiction which already has been stated ten years before Condon's contribution by Hund [19] known as Hund's paradox: stable ground energy states of chiral molecules with respect to a two-well potential are achiral, whereas the L- and R-states formed by eigenstates associated with the two local minima are not stationary and can tunnel through the potential barrier such that an enantiomer should permanently switch between its L- and R-form. Obviously, there must be an additional coupling effect which destabilizes the achiral ground state of quantum mechanics and stabilizes the L- and R-form once the molecule has been synthesized accordingly. A possible effect is provided by electro-weak quantum chemistry: thirty years ago, computations revealed that there is an energy difference between L- and R-form enantiomers in achiral media ('parity violation' resp. 'de lege symmetry breaking') which dominates the tunneling effect. This result is of significant relevance for the understanding of molecular chirality: only in case of parity violation the R- and L-form of enantiomers can be observed in an absolute sense (cf., e.g., [32]). The current status of spectroscopic experiments, confirming molecular parity violation, is reviewed in [33].

Nowadays, enantiomer separation and enantiomer selectivity play a significant role in agrochemical, electronic, and pharmaceutical as well as food, flavor and fragrance industries (cf., e.g., [2, 8, 9, 13, 23, 29]). The relevance of chirality in drug design became apparent on occasion of the so-called 'Contergan scandal' or 'thalidomide disaster' in the sixties of the last century when worldwide thousands of children were born with extremely severe deformities after their mothers had taken this sleeping drug in early pregnancy. Unfortunately, it was discovered too late that L-thalidomide molecules cause malformations of the fetus, since they block the action of a chiral enzyme regulating the synthesis of cartilage in the second month of the pregnancy. The qualitative and quantitative analysis of chiral molecules relies on high-throughput screening by fluorescence spectroscopy and mass spectroscopy with achiral reporter molecules or antibodies and enzymes [7]. Since the chemical synthesis of enantiomers usually gives rise to racemic compounds, chiral separation is of utmost importance. Current approaches are based on direct gas chromatography [7] or HPLC (High Pressure Liquid Chromatography) [39], capillary electrophoresis [34], or NMR (Nuclear Magnetic Resonance) anisotropy methods [40]. They suffer from the drawbacks that they are slow and only yield endpoint results, i.e., they do not provide any information about the dynamics of the separation process. Moreover, they mostly require costly chiral media. Consequently, in order to guarantee a higher cost-effectiveness as well as a significant speed-up and to allow for an in-situ investigation of the enantiomer separation at a high time-resolution, there is the need for alternative techniques. Such techniques have been provided by chiral separation in microfluidic devices taking advantage of the fact that enantiomers drift in microflows with a direction depending on their chirality (cf., e.g., [7, 21, 22, 25, 26, 35]).

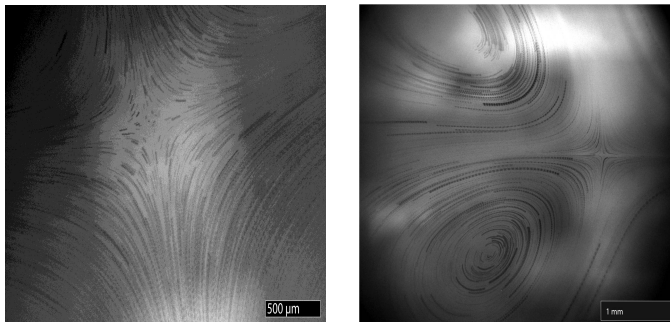


FIG. 1.2. *Left: Vorticity pattern at the surface of the fluid. The optical path is slightly tilted to gain a larger field of view. The image is a superposition of micrographs and shows parts of the four quadrant flows induced by the SAWs. Right: Micrograph showing two of the counter-rotating vortices. In the flow quadrant diagonally opposing vortices always have the same direction of rotation.*

In this paper, we are concerned with the separation of deformable vesicle-like enantiomers by a specific flow pattern generated by surface acoustic waves (SAWs). The experimental set-up consists of a fluid-filled container with an immersed SAW microchip at the ground. The SAW microchip is coated with a piezoelectric material such as lithium niobate (LiNbO_3) and features an Inter-Digital Transducer (IDT) placed at the center of the bottom of the container with its aperture pointing upwards (cf. Figure 1.3 (left)). Applying a high-frequency signal to the IDT, acoustic waves are generated that enter the fluid in the container and create a steady-state

flow pattern at the fluid surface consisting of four counter-rotating vortices (cf. Figure 1.2 and Figure 1.3 (right)). Almost flat L-shaped enantiomers with hydrophobic top and bottom are injected onto the surface of the fluid between two counter-rotating vortices. It turns out that right-handed (left-handed) enantiomers get trapped by left-rotating (right-rotating) vortices in the sense that they stably rotate around the center of the vortex.

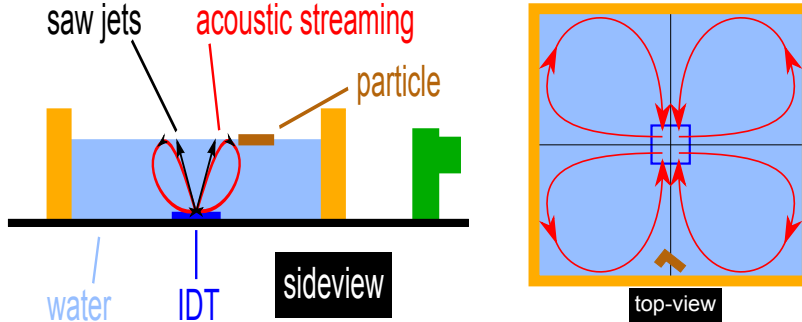


FIG. 1.3. *Left: Schematic sideview of the experimental setup. Right: Topview of the vorticity pattern created at the fluid surface.*

For the numerical simulation of the surface acoustic wave actuated enantiomer separation we have used the Finite Element Immersed Boundary Method (FE-IB). The Immersed Boundary Method (IB) is due to Peskin [30] (cf. the survey paper [31] and the references therein) and has been extended to the FE-IB in [4, 5] (cf. also [14, 18]). The FE-IB is based on a coupled system consisting of the incompressible Navier-Stokes equations described in an Eulerian coordinate system and the equation of motion of the immersed enantiomer described with respect to a Lagrangian coordinate system.

The paper is organized as follows: Section 2 is devoted to a description of the FE-IB, whereas section 3 deals with its numerical realization. Finally, section 4 contains the results of numerical simulations illustrating the feasibility of SAW actuated enantiomer separation.

2. The Finite Element Immersed Boundary Method. In this section, we adopt standard notation from Lebesgue and Sobolev space theory (cf., e.g., [36]). In particular, for $D \subset \mathbb{R}^2$ we refer to $L^2(D)$ and $H^s(D)$ as the Hilbert space of Lebesgue integrable functions in D with inner product $(\cdot, \cdot)_{0,D}$ and associated norm $\|\cdot\|_{0,D}$ and the Sobolev space of functions with inner product $(\cdot, \cdot)_{s,D}$ and norm $\|\cdot\|_{s,D}$. $L_0^2(D)$ is the subspace of functions with zero integral mean. We further refer to $H_0^1(D)$ as the closure of $C_0^\infty(D)$ in $H^1(D)$ and to $H^{-1}(D)$ as the dual of $H_0^1(D)$, denoting by $\langle \cdot, \cdot \rangle_{H^{-1}, H_0^1}$ the dual pairing. For $\Sigma \subseteq \partial D$ and a function $v \in H^s(D)$, we denote by $v|_\Sigma$ the trace of v on Σ . We write $\mathbf{L}^2(D)$ and $\mathbf{H}^s(D)$ in case of vector-valued functions.

Since the enantiomers float on the surface $\Omega := (0, L)^2$, $L > 0$, of the fluid, we are only interested in the fluid flow and the motion of the enantiomers in Ω . The fluid flow in Ω can be modeled by the incompressible Navier-Stokes equations with a source term $\mathbf{f} = \mathbf{f}_q + \mathbf{f}_g$ consisting of a quadrupolar force density \mathbf{f}_q , reflecting the SAW induced vorticity pattern on Ω , and a global force density \mathbf{f}_g , reflecting the impact of the

enantiomers on the flow:

$$\rho_f \frac{\partial \mathbf{v}}{\partial t} + \rho(\mathbf{v} \cdot \nabla) \mathbf{v} - \eta \Delta \mathbf{v} + \nabla p = \mathbf{f} \quad \text{in } \Omega \times (0, T), \quad (2.1a)$$

$$\nabla \cdot \mathbf{v} = 0 \quad \text{in } \Omega \times (0, T), \quad (2.1b)$$

$$\mathbf{v} = \mathbf{0} \quad \text{on } \partial\Omega \times [0, T], \quad (2.1c)$$

$$\mathbf{v}(\cdot, 0) = \hat{\mathbf{v}} \quad \text{in } \Omega. \quad (2.1d)$$

The quadrupolar force density \mathbf{f}_q and $\hat{\mathbf{v}}$ are given according to

$$\mathbf{f}_q := -\eta \Delta \hat{\mathbf{v}}, \quad \hat{\mathbf{v}} = (\hat{v}_1, \hat{v}_2)^T, \quad \hat{v}_1 = \partial \Psi / \partial x_1, \quad \hat{v}_2 = -\partial \Psi / \partial x_2 \quad (2.2)$$

in terms of the stream function

$$\Psi(x_1, x_2) = v_0(f) L \frac{\sin(\pi x_1 / L) \sin(\pi x_2 / L)}{(2 - \cos(\pi x_1 / L)) (2 - \cos(\pi x_2 / L))}, \quad (2.3)$$

where $v_0(f) > 0$ depends on the frequency f of the IDT. We note that \mathbf{f}_q provides a good approximation of the SAW generated vorticity pattern at the surface of the fluid (cf. Figure 4.2 in section 4). The global force density \mathbf{f}_g will be specified by means of the total energy of the immersed boundary in (2.6) below.

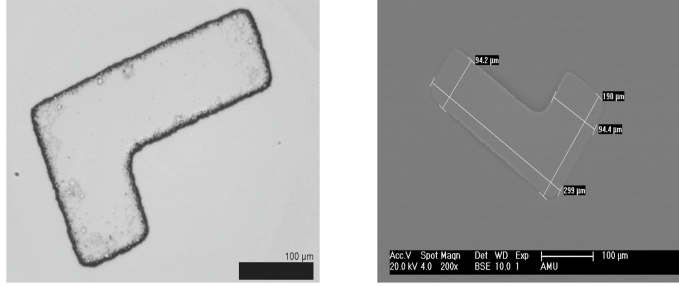


FIG. 2.1. Micrograph of a photoresist L-shaped enantiomer (left) and its length scales (right).

In the FE-IB an immersed enantiomer is modeled as a body consisting of an elastic membrane enclosing a fluid which here is assumed to have the same density and viscosity as the carrier fluid in the container. In practice, this can be achieved by density and viscosity matching, i.e., adding chemical additives to the carrier fluid. The immersed enantiomer is supposed to occupy a subdomain $B_t \subset \Omega$, $t \in [0, T]$, with boundary ∂B_t which is a non-selfintersecting closed curve. We further assume that the boundary ∂B_0 of the initial configuration B_0 has length $\ell := |\partial B_0|$ and denote by $q \in [0, \ell]$ the Lagrangian coordinate labeling a material point on ∂B_0 . Figure 2.1 shows the micrograph of a photoresist right-handed L-shaped enantiomer (left) and its length scales (right). Here, the perimeter ℓ of the enantiomer is $\ell = 8.78 \cdot 10^{-4} m$. We refer to $\mathbf{X}(q, t) = (X_1(q, t), X_2(q, t))^T$ as the position vector of the point q at time $t \in (0, T]$ which moves with the velocity \mathbf{v} of the fluid such that the equation of motion takes the form

$$\frac{d\mathbf{X}}{dt}(q, t) = \mathbf{v}(\mathbf{X}(q, t), t), \quad q \in [0, \ell], \quad t \in [0, T], \quad (2.4a)$$

$$\mathbf{X}(q, 0) = \mathbf{X}^0(q), \quad q \in [0, \ell], \quad (2.4b)$$

where \mathbf{X}^0 stands for the initial position.

The total elastic energy of the immersed boundary ∂B_t of the enantiomer is given by

$$E(t) := E^e(t) + E^b(t), \quad t \in (0, T), \quad (2.5)$$

$$E^e(t) := \int_0^\ell \mathcal{E}^e(\mathbf{X}(q, t)) dq, \quad E^b(t) := \int_0^\ell \mathcal{E}^b(\mathbf{X}(q, t)) dq,$$

where $\mathcal{E}^e(t)$ and $\mathcal{E}^b(t)$ are the local energy densities with respect to elongation-compression and bending. Denoting by \mathbf{f}_i the local force density according to $\mathbf{f}_i(q, t) = -E'(\mathbf{X}(q, t))$, where E' is the Gâteaux derivative of E , the global force density \mathbf{f}_g in (2.1a) is given in variational form by

$$\langle \mathbf{f}_g(t), \mathbf{w} \rangle_{\mathbf{H}^{-1}, \mathbf{H}_0^1} = \int_0^\ell \mathbf{f}_i(q, t) \cdot \mathbf{w}(\mathbf{X}(q, t)) dq, \quad \mathbf{w} \in \mathbf{H}_0^1(\Omega). \quad (2.6)$$

The FE-IB is based on the variational formulation of (2.1) and (2.4). To this end, we introduce the function spaces

$$\begin{aligned} \mathbf{V}(0, T) &:= \mathbf{H}^1((0, T), \mathbf{H}^{-1}(\Omega)) \cap \mathbf{L}^2((0, T), \mathbf{H}^1(\Omega)), \\ \mathbf{W}(0, T) &:= \{\mathbf{v} \in \mathbf{V}(0, T) \mid \mathbf{v}|_{\partial\Omega} = \hat{\mathbf{v}}\}, \\ Q(0, T) &:= L^2((0, T), L_0^2(\Omega)), \\ \mathbf{Y}(0, T) &:= \mathbf{H}^1((0, T), \mathbf{L}^2([0, \ell])) \cap \mathbf{L}^2((0, T), \mathbf{H}_{\text{per}}^3([0, \ell])), \end{aligned}$$

where $\mathbf{H}_{\text{per}}^3([0, \ell]) := \{\mathbf{Y} \in \mathbf{H}^3((0, \ell)) \mid \partial^k \mathbf{Y}(0)/\partial q^k = \partial^k \mathbf{Y}(\ell)/\partial q^k, k = 0, 1, 2\}$.

The weak formulation of the Navier-Stokes equations (2.1) requires the computation of $(\mathbf{v}, p) \in \mathbf{W}(0, T) \times Q(0, T)$ such that for all $\mathbf{w} \in \mathbf{H}_0^1(\Omega)$ and all $q \in L_0^2(\Omega)$ there holds

$$\langle \rho \frac{\partial \mathbf{v}}{\partial t}, \mathbf{w} \rangle_{\mathbf{H}^{-1}, \mathbf{H}_0^1} + a(\mathbf{v}, \mathbf{w}) - b(p, \mathbf{w}) = \ell(\mathbf{w}), \quad (2.7a)$$

$$b(q, \mathbf{v}) = 0, \quad (2.7b)$$

$$(\mathbf{v}(\cdot, 0), \mathbf{w})_{0, \Omega} = (\hat{\mathbf{v}}, \mathbf{w})_{0, \Omega}. \quad (2.7c)$$

Here, $a(\cdot, \cdot)$, $b(\cdot, \cdot)$, and the functional $\ell(\cdot)$ are given by

$$a(\mathbf{v}, \mathbf{w}) := (\rho_f(\mathbf{v} \cdot \nabla) \mathbf{v}, \mathbf{w})_{0, \Omega} + (\eta \nabla \mathbf{v}, \nabla \mathbf{w})_{0, \Omega} \quad (2.8a)$$

$$b(p, \mathbf{v}) := (p, \nabla \cdot \mathbf{v})_{0, \Omega}, \quad \ell(\mathbf{w}) := (\mathbf{f}_q, \mathbf{w})_{0, \Omega} + \langle \mathbf{f}_g, \mathbf{w} \rangle_{\mathbf{H}^{-1}, \mathbf{H}_0^1}. \quad (2.8b)$$

On the other hand, the weak formulation of (2.4) amounts to the computation of $\mathbf{X} \in \mathbf{Y}(0, T)$ such that for all $\mathbf{Z} \in \mathbf{H}_{\text{per}}^3([0, \ell])$ it holds

$$\left(\frac{d\mathbf{X}}{dt}(\cdot, t), \mathbf{Z} \right)_{0, (0, \ell)} = (\mathbf{v}(\mathbf{X}(\cdot, t), t), \mathbf{Z})_{0, (0, \ell)}, \quad t \in [0, T], \quad (2.9a)$$

$$(\mathbf{X}(\cdot, 0), \mathbf{Z})_{0, (0, \ell)} = (\mathbf{X}^0, \mathbf{Z})_{0, (0, \ell)}. \quad (2.9b)$$

3. The Backward Euler/Forward Euler FE-IB. For the discretization in space of the incompressible Navier-Stokes equations (2.7) we use Taylor-Hood P2/P1 elements with respect to a quasi-uniform simplicial triangulation $\mathcal{T}_h(\Omega)$ of Ω . For

$K \in \mathcal{T}_h(\Omega)$, we denote by $|K|$ the area of K , by h_K the diameter of K , and we set $h := \max\{h_K \mid K \in \mathcal{T}_h(\Omega)\}$. Further, $P_k(K)$, $k \in \mathbb{N}$, refers to the set of polynomials of degree $\leq k$ on K . The associated finite element spaces \mathbf{V}_h for the velocity and Q_h for the pressure read

$$\begin{aligned}\mathbf{V}_h &:= \{\mathbf{v}_h \in \mathbf{C}(\bar{\Omega}) \mid \mathbf{v}_h|_K \in P_2(K)^2, K \in \mathcal{T}_h(\Omega), \mathbf{v}_h|_{\partial\Omega} = \hat{\mathbf{v}}_h\}, \\ Q_h &:= \{w_h \in C(\bar{\Omega}) \mid w_h|_K \in P_1(K), K \in \mathcal{T}_h(\Omega), \int_{\Omega} w_h dx = 0\},\end{aligned}$$

where $\hat{\mathbf{v}}_h$ is the \mathbf{L}^2 -projection of $\hat{\mathbf{v}}$ onto the space of piecewise polynomials of degree 2 on $\partial\Omega$. For the discretization of the boundary of the immersed enantiomer we consider a partition

$$\mathcal{T}_{\Delta q} := \{0 =: q_0 < q_1 < \dots < q_R := \ell\}, \quad R \in \mathbb{N},$$

of the interval $[0, \ell]$ into subintervals $I_i := [q_{r-1}, q_r]$, $1 \leq r \leq R$, of length $\Delta q_r := q_r - q_{r-1}$ with $\Delta q := \max\{\Delta q_r \mid 1 \leq r \leq R\}$. We approximate \mathbf{X} from (2.9) by periodic cubic splines

$$\begin{aligned}\mathbf{S}_h &:= \{\mathbf{Z}_h \in \mathbf{C}^2([0, \ell]) \mid \mathbf{Z}_h|_{I_r} \in P_3(I_r)^2, 1 \leq r \leq R, \\ &\quad \mathbf{Z}_h^{(k)}(q_0) = \mathbf{Z}_h^{(k)}(q_R), k = 0, 1, 2\},\end{aligned}$$

where $P_3(I_r)$ stands for the set of polynomials of degree ≤ 3 on I_r . For $\mathbf{Z}_h \in \mathbf{S}_h$, we set $\mathbf{Z}_r := \mathbf{Z}_h(q_r)$, $0 \leq r \leq R$. The discrete immersed enantiomer occupies subdomains $B_{h,t} \subset \Gamma_s$ with boundaries $\partial B_{h,t}$ that are C^2 curves parameterized by the periodic cubic spline $\mathbf{X}_h(\cdot, t) \in \mathbf{S}_h$.

We define the discrete elastic energy $E_h^e(t)$ and the discrete bending energy $E_h^b(t)$ according to

$$E_h^e(t) = \frac{\kappa_e}{2} \int_0^\ell \left(\left| \frac{\partial \mathbf{X}_h}{\partial q}(q, t) \right|^2 - 1 \right) dq, \quad (3.1a)$$

$$E_h^b(t) = \frac{\kappa_b}{2} \sum_{r=1}^R \int_{q_{r-1}}^{q_r} \left| \frac{\partial^2 \mathbf{X}_h}{\partial q^2}(q, t) \right|^2 dq. \quad (3.1b)$$

Observing that $\partial^3 \mathbf{X}_h(q, t) / \partial q^3$ is constant on I_r , the discrete force density takes the form

$$\begin{aligned}\langle \mathbf{f}_{h,g}(\cdot, t), \mathbf{w}_h \rangle_h &= -\kappa_e \int_0^\ell \frac{\partial \mathbf{X}_h(q, t)}{\partial q} \cdot \frac{\partial}{\partial q} \mathbf{w}_h(\mathbf{X}_h(q, t)) dq \\ &+ \kappa_b \sum_{i=1}^R \int_{q_{i-1}}^{q_i} \frac{\partial^3 \mathbf{X}_h(q, t)}{\partial q^3} \cdot \frac{\partial}{\partial q} \mathbf{w}_h(\mathbf{X}_h(q, t)) dq = \\ &- \kappa_e \int_0^\ell \frac{\partial \mathbf{X}_h(q, t)}{\partial q} \cdot \nabla \mathbf{w}_h(\mathbf{X}_h(q, t)) \frac{\partial \mathbf{X}_h(q, t)}{\partial q} dq \\ &+ \kappa_b \sum_{r=1}^R \frac{\partial^3 \mathbf{X}_h(q, t)}{\partial q^3} \Big|_{I_r} \cdot \int_{q_{r-1}}^{q_r} \nabla \mathbf{w}_h(\mathbf{X}_h(q, t)) \frac{\partial \mathbf{X}_h(q, t)}{\partial q} dq.\end{aligned} \quad (3.2)$$

We thus obtain the following approximation of the right-hand side in (2.7a)

$$\ell_h(\mathbf{w}_h, t) := (\mathbf{f}_q, \mathbf{w}_h)_{0,(0,\ell)} + \langle \mathbf{f}_{h,g}(\cdot, t), \mathbf{w}_h \rangle_h. \quad (3.3)$$

The discretization in time is done with respect to an equidistant partition

$$\mathcal{T}_{\Delta t} := \{0 =: t_0 < t_1 < \dots < t_M := T\}, \quad M \in \mathbb{N},$$

of the time interval $[0, T]$ into subintervals of length $\Delta t := T/M$. We denote by $\mathbf{v}_h^{(m)}$ an approximation of $\mathbf{v}_h \in \mathbf{V}_h$ at $t = t_m$. We further refer to $\mathbf{D}_{\Delta t}^+ \mathbf{v}_h^{(m)} := (\mathbf{v}_h^{(m+1)} - \mathbf{v}_h^{(m)})/(\Delta t)$ and $\mathbf{D}_{\Delta t}^- \mathbf{v}_h^{(m)} := (\mathbf{v}_h^{(m)} - \mathbf{v}_h^{(m-1)})/(\Delta t)$ as the forward and backward difference operator. We set

$$\begin{aligned} \mathbf{W}_h^{(m)} &:= \{\mathbf{w}_h^{(m)} \in \mathbf{C}(\bar{\Gamma}_s) \mid \mathbf{w}_h^{(m)} \in \mathbf{V}_h, \mathbf{w}_h^{(m)}|_{\partial\Gamma_s} = \hat{\mathbf{v}}_h\}, \\ Q_h^{(m)} &:= \{w_h^{(m)} \in C(\bar{\Gamma}_s) \mid w_h^{(m)}|_K \in Q_h, \int_{\Gamma_s} w_h^{(m)} dx = 0\}. \end{aligned}$$

The Backward Euler/Forward Euler FE-IB reads as follows: Given $\mathbf{v}_h^{(0)} = \hat{\mathbf{v}}_h$ and $\mathbf{X}_h^{(0)} \in \mathbf{S}_h$, for $m = 0, \dots, M-1$ we perform the following two steps:

Step 1: Compute $(\mathbf{v}_h^{(m+1)}, p_h^{(m+1)}) \in \mathbf{W}_h^{(m+1)} \times Q_h^{(m+1)}$ such that for all $\mathbf{w}_h \in \mathbf{V}_{h,0} := \{\mathbf{w}_h \in \mathbf{V}_h \mid \mathbf{w}_h|_{\partial\Gamma_s} = \mathbf{0}\}$ it holds

$$(\rho_f \mathbf{D}_{\Delta t}^+ \mathbf{v}_h^{(m)}, \mathbf{w}_h)_{0,\Gamma_s} + a(\mathbf{v}_h^{(m+1)}, \mathbf{w}_h) - b(p_h^{(m+1)}, \mathbf{w}_h) = \ell_h^{(m)}(\mathbf{w}_h), \quad (3.4a)$$

$$b(w_h, \mathbf{v}_h^{(m+1)}) = 0, \quad (3.4b)$$

where $\ell_h^{(m)}(\mathbf{w}_h) := \ell_h(\mathbf{w}_h, t_m)$ is given by (3.3).

Step 2: Compute $\mathbf{X}_h^{(m+1)} \in \mathbf{S}_h$ such that for all $\mathbf{Z}_h \in \mathbf{S}_h$ it holds

$$(\mathbf{D}_{\Delta t}^+ \mathbf{X}_r^{(m)}, \mathbf{Z}_h)_{0,(0,\ell)} = (\mathbf{v}_h^{(m+1)}(\mathbf{X}_r^{(m)}), \mathbf{Z}_h)_{0,(0,\ell)}, \quad 1 \leq r \leq R. \quad (3.5)$$

As has been shown in [14, 18], the Backward Euler/Forward Euler FE-IB is not unconditionally stable, but has to satisfy the CFL-type stability condition

$$\frac{\Delta t}{h} \leq \frac{\eta}{4C(\kappa_e L_1 + \kappa_b L_2)}, \quad (3.6)$$

where $C > 0$ is a constant depending on the size and shape of the immersed enantiomer and L_1, L_2 are given by

$$L_1 := \max_{0 \leq m \leq M} \max_{q \in [0,\ell]} \left| \frac{\partial \mathbf{X}_h^{(m)}}{\partial q} \right|, \quad L_2 := \max_{0 \leq m \leq M} \max_{1 \leq r \leq R} \left| \frac{\partial^3 \mathbf{X}_h^{(m)}}{\partial q^3} \right|_{I_r}.$$

A widely used spring-model [37, 38] for the immersed body can be easily derived from the discrete model introduced above. We approximate the boundary $\partial B_{h,t}$ of an immersed enantiomer by a closed polygon with vertices $\mathbf{X}_i(t) = \mathbf{X}_h(q_i, t)$, $0 \leq i < R$, and denote by $D_{\Delta q}^\pm \mathbf{X}_i(t)$ the forward and backward difference quotient as given by

$$\mathbf{D}_{\Delta q}^+ \mathbf{X}_i(t) := \frac{\mathbf{X}_{i+1}(t) - \mathbf{X}_i(t)}{\Delta q_{i+1}}, \quad \mathbf{D}_{\Delta q}^- \mathbf{X}_i(t) := \frac{\mathbf{X}_i(t) - \mathbf{X}_{i-1}(t)}{\Delta q_i}. \quad (3.7)$$

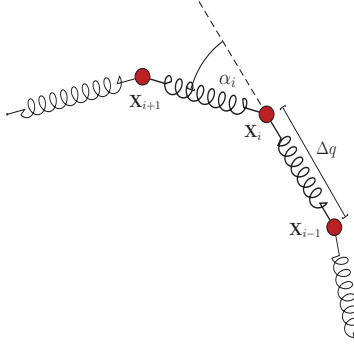


FIG. 3.1. A spring model for the immersed enantiomer

We assume that the vertices are connected by elastic springs (cf. Figure 3.1) with spring constants $\kappa_e > 0$. Replacing $\partial \mathbf{X}_h / \partial q$ in (3.1a) with its approximation $D_{\Delta q}^+ \mathbf{X}_i$ by the forward difference quotient and the integral in (3.1a) by the simplest quadrature rule, we obtain the following discrete model for the dilation elastic energy:

$$E_h^e(t) = \frac{\kappa_e}{2} \sum_{i=0}^{R-1} \left(|D_{\Delta q}^+ \mathbf{X}_i(t)| - 1 \right)^2 \Delta q_{i+1}. \quad (3.8)$$

Likewise, replacing the second derivative $\partial^2 \mathbf{X}_h / \partial q^2$ in (3.1b) with its approximation $D_{\Delta q}^2 \mathbf{X}_i$ by the central difference quotient $D_{\Delta q}^2 \mathbf{X}_i := D_{\Delta q}^+ D_{\Delta q}^- \mathbf{X}_i$ and the integral in (3.1b) by the trapezoidal rule, for the bending energy we get:

$$E_h^b(t) = \frac{\kappa_b}{2} \sum_{i=1}^R |D_{\Delta q}^2 \mathbf{X}_i(t)|^2 \Delta q_i, \quad (3.9)$$

where $\mathbf{X}_{R+i} := \mathbf{X}_i, 1 \leq i \leq 2$, and $\mathbf{X}_{-1} := \mathbf{X}_{R-1}$. In case $\Delta q_i = \Delta q, 1 \leq i \leq R$, a simple calculation reveals

$$\begin{aligned} |D_{\Delta q}^2 \mathbf{X}_i(t)|^2 &= (\Delta q)^{-4} |(\mathbf{X}_{i+1} - \mathbf{X}_i)(t)| |(\mathbf{X}_i - \mathbf{X}_{i-1})(t)| \cdot \\ &\quad \left(\frac{|(\mathbf{X}_{i+1} - \mathbf{X}_i)(t)|}{|(\mathbf{X}_i - \mathbf{X}_{i-1})(t)|} + \frac{|(\mathbf{X}_i - \mathbf{X}_{i-1})(t)|}{|(\mathbf{X}_{i+1} - \mathbf{X}_i)(t)|} - 2\cos(\alpha_i(t)) \right), \end{aligned}$$

where $\alpha_i(t)$ is the angle formed by the vectors $(\mathbf{X}_{i+1} - \mathbf{X}_i)(t)$ and $(\mathbf{X}_i - \mathbf{X}_{i-1})(t)$ (cf. Figure 3.1), i.e.,

$$\cos(\alpha_i(t)) = \frac{(\mathbf{X}_{i+1} - \mathbf{X}_i)(t) \cdot (\mathbf{X}_i - \mathbf{X}_{i-1})(t)}{|(\mathbf{X}_{i+1} - \mathbf{X}_i)(t)| |(\mathbf{X}_i - \mathbf{X}_{i-1})(t)|}.$$

Assuming $|(\mathbf{X}_{i+1} - \mathbf{X}_i)(t)| \approx |(\mathbf{X}_i - \mathbf{X}_{i-1})(t)|$ and using $\sin^2(\alpha_i(t)/2) = (1 - \cos(\alpha_i(t)))/2$, it follows that

$$\begin{aligned} |D_{\Delta q}^2 \mathbf{X}_i(t)|^2 &\approx \\ 4(\Delta q)^{-4} &|(\mathbf{X}_{i+1} - \mathbf{X}_i)(t)| |(\mathbf{X}_i - \mathbf{X}_{i-1})(t)| \sin^2(\alpha_i(t)/2). \end{aligned}$$

Hence, introducing local bending rigidities

$$\kappa_b^{(i)} := \kappa_b \frac{|(\mathbf{X}_{i+1} - \mathbf{X}_i)(t)|}{\Delta q} \frac{|(\mathbf{X}_i - \mathbf{X}_{i-1})(t)|}{\Delta q} \cos^2(\alpha_i(t)/2),$$

we obtain

$$E_h^b(t) = \frac{1}{2} \sum_{i=1}^R \kappa_b^{(i)} \left(\frac{\tan(\alpha_i(t)/2)}{2\Delta q} \right)^2 \Delta q. \quad (3.10)$$

Since the immersed L-shaped enantiomers are only slightly deformable and feature a different bending behavior at the corner points, the discrete bending energy has to be modified such that the deviation from prescribed angles α_i^d , $1 \leq i \leq R$, is minimized. We use

$$E_h^b(t) = \frac{1}{2} \sum_{i=1}^R \kappa_b^{(i)} \left(\frac{\tan((\alpha_i(t) - \alpha_i^d)/2)}{2\Delta q} \right)^2 \Delta q, \quad (3.11)$$

where the angles α_i^d and the local bending rigidities $\kappa_b^{(i)}$ are given by

$$\begin{aligned} \alpha_i^d &:= \begin{cases} \pi/2 & \text{at corner points} \\ 0 & \text{otherwise} \end{cases}, \\ \kappa_b^{(i)} &:= \kappa_b \kappa_i \frac{|(\mathbf{X}_{i+1} - \mathbf{X}_i)(t)|}{\Delta q} \frac{|(\mathbf{X}_i - \mathbf{X}_{i-1})(t)|}{\Delta q} \cos^2((\alpha_i(t) - \alpha_i^d)/2), \\ \kappa_i &:= \begin{cases} 2.7 & \text{for corner points} \\ 1 & \text{otherwise} \end{cases}, 1 \leq i \leq R. \end{aligned} \quad (3.12)$$

4. Numerical results. We present the results of numerical simulations of the separation of photoresist L-shaped enantiomers by SAW generated vorticity patterns consisting of four pairwise counter-rotating vortices at the surface of the fluid.

The production of the photoresist L-shaped enantiomers is shown in Figure 4.1. A sacrificial layer of omnicoat is spincoated on a silicon wafer followed by a second spin coating process where SU8-2 photoresist laden with 0.5mg/ml Nile Red is spun onto the omnicoat layer at 3000 rounds per second achieving a film thickness of about 1.5 μm . After soft baking, the photoresist is exposed using a mask aligner and then baked a second time. Then the substrate is cooled to room temperature and the unexposed photoresist is developed using MR-DEV300 leaving the desired particles attached to the sacrificial layer of omnicoat. In order to render the particles hydrophobic on one side, a layer of Trichloro(octadecyl)silane (OTS) is applied by spin coating. To this end 10 μl OTS are dissolved in 3ml n-hexane and spun onto the particles at 1000 rpm for 10 seconds. The layer of OTS renders the particles highly hydrophobic on the top side. After these steps the particles are still firmly attached to the substrate. To remove the particles from the wafer a lift-off procedure is performed using omnicoat developer. The wafer is immersed in the solution until the omnicoat layer has been sufficiently dissolved. The wafer is then transferred to the experimental setup and the detached particles can be washed off using pure water. Due to the top side of the particles being considerably more hydrophobic than the bottom side the orientation of the particles is conserved during the lift off process and the particles float stably on the surface of the fluid.

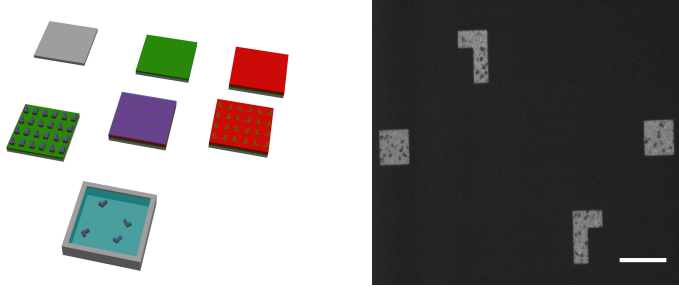


FIG. 4.1. Schematic representation of the fabrication of photoresist particles (left) and microparticles of different shapes still attached to the silicon wafer. The scalebar represents $300\mu\text{m}$ (right).

The material data and the numerical data have been chosen as follows:

The fluid with density $\rho_f = 1.1 \cdot 10^3 \text{ kg/m}^3$ and the viscosity $\eta = 1.01 \cdot 10^{-6} \text{ m}^2/\text{s}$ occupied a domain $D = (0, L)^2 \times (0, H)$ with $L = 4.0 \cdot 10^{-2} \text{ m}$ and $H = 5.0 \cdot 10^{-3} \text{ m}$. The material moduli of the enantiomers were given by $\kappa_e = 3.0 \cdot 10^{-2} \text{ N/m}$ and $\kappa_b = 2.5 \cdot 10^{-17} \text{ Nm}$, and we used a spring model (cf. (3.11) with $\alpha_i^d, \kappa_i, 1 \leq i \leq R$, as in (3.12).

The operating frequency f of the IDT was chosen according to $f = 1.42 \cdot 10^2 \text{ MHz}$. The associated parameter $v_0(f)$ in (2.3) has been calibrated on the basis of an experimentally measured flow field. It turned out that $v_0(f) = 2.0 \cdot 10^{-3} \text{ m/s}$ provided a good approximation of the resulting velocity pattern at the surface of the fluid (cf. Figure 4.2).

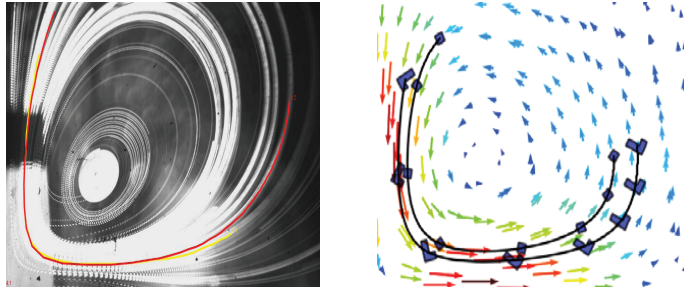


FIG. 4.2. Experimentally measured flow field and trajectories (left) and numerically computed flow field and trajectories (right) in the upper right quadrant of the fluid surface (for square shaped and L-shaped photoresist particles).

For the numerical solution of the coupled system (2.7),(2.9) by the Backward Euler/Forward Euler FE-IB we have used different uniform simplicial triangulations of the surface of the fluid by right isosceles with $h \in \{L/20, L/30, L/40\}$ and different uniform partitions of $[0, \ell]$ with $\Delta q \in \{1/100, 1/200, 1/400\}$. We have further used a uniform partition of the time interval with time step size $\Delta t = 1/2000$ satisfying the CFL-condition (3.6). All computations have been performed under Linux featuring Intel(R)Core(TM) i3-2100 CPU 3.10 GHz and 7.7 GB RAM.

Simulation Results: Since the different meshes for Ω and partitions of $[0, \ell]$ produced essentially identical trajectories of the enantiomers, the following simulation

results, displayed in Figures 4.3-4.5, are those obtained for $h = L/40$, $\Delta q = 1/200$, and $\Delta t = 1/2000$.

Five left-handed L-shaped enantiomers have been injected onto the surface of the fluid approximately in the middle between two counter-rotating vortices. The motion of the enantiomers is such that they get attracted by the right-rotating fluid vortex. After the completion of the first cycle around the center of the vortex, new cycles begin with paths of the enantiomers similar to the first one (cf. Figure 4.3). Figure 4.4 displays the paths of five right-handed L-shaped enantiomers which get attracted by the left-rotating vortex. A more realistic scenario is displayed in Figure 4.5 with two right-handed and two left-handed L-shaped enantiomers initially placed in the middle between the lower two counter-rotating vortices. The upper left-handed enantiomer and the upper right-handed enantiomer get attracted by the upper left right-rotating and the upper right left-rotating vortex, whereas the lower right-handed enantiomer and the lower left-handed enantiomer circle around the lower left left-rotating and the lower right right-rotating vortex, respectively. We emphasize that also in this case we achieve a perfect separation in the sense that left-handed/right-handed enantiomers get attracted by right-rotating/left-rotating vortices.

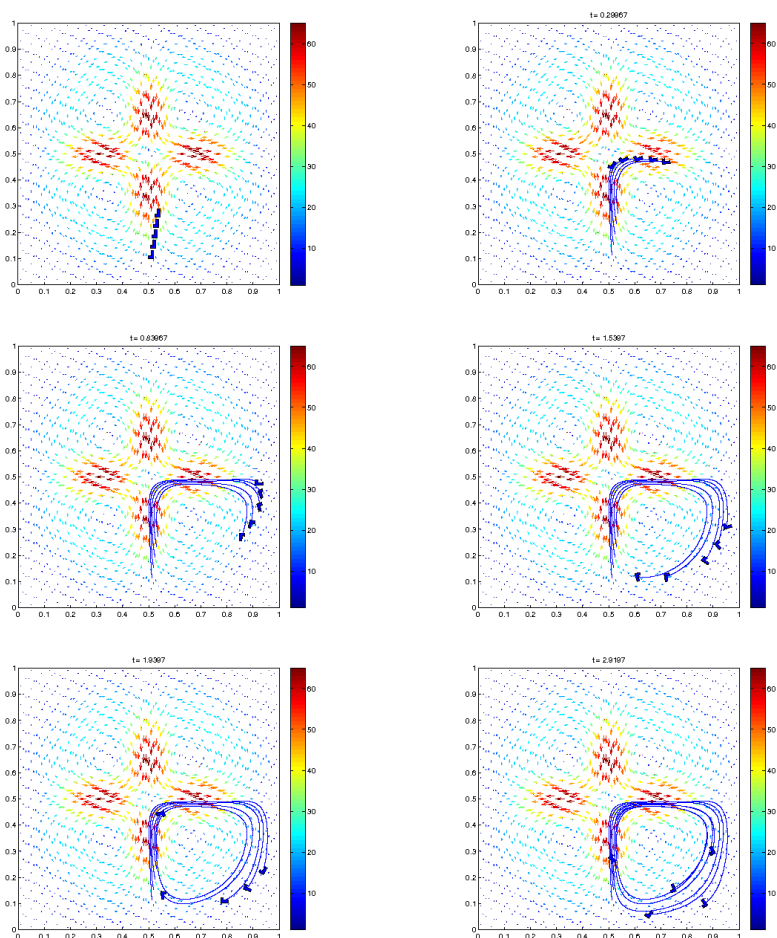


FIG. 4.3. Velocity field and motion of five left-handed *L*-shaped enantiomers initially placed in the middle between two counter-rotating vortices

REFERENCES

- [1] H. Antil, R. Glowinski, R. H. W. Hoppe, C. Linsenmann, T.-W. Pan, and A. Wixforth; *Modeling, simulation, and optimization of surface acoustic wave driven microfluidic biochips*. *J. Comp. Math.* **28**, 149–169, 2010.
- [2] K. Bester; *Chiral analysis for environmental applications*. *Anal. Bioanal. Chem.* **376**, 302–304, 2003.
- [3] J.-B. Biot; *Bull. Soc. Philomath.* **6**, 190–192, 1815
- [4] D. Boffi and L. Gastaldi; *A finite element approach for the immersed boundary method*. *Comput. Struct.* **81**, 491–501, 2003.
- [5] D. Boffi, L. Gastaldi, and L. Heltai; *Numerical stability of the finite element immersed boundary method*. *Math. Models and Methods in Appl. Sci.* **17**, 1479–1505, 2007.
- [6] M. Born; *Electron theory of natural optic rotation processes in isotropic and anisotropic liquids*. *Ann. Phys.* **55**, 177–240, 1918.

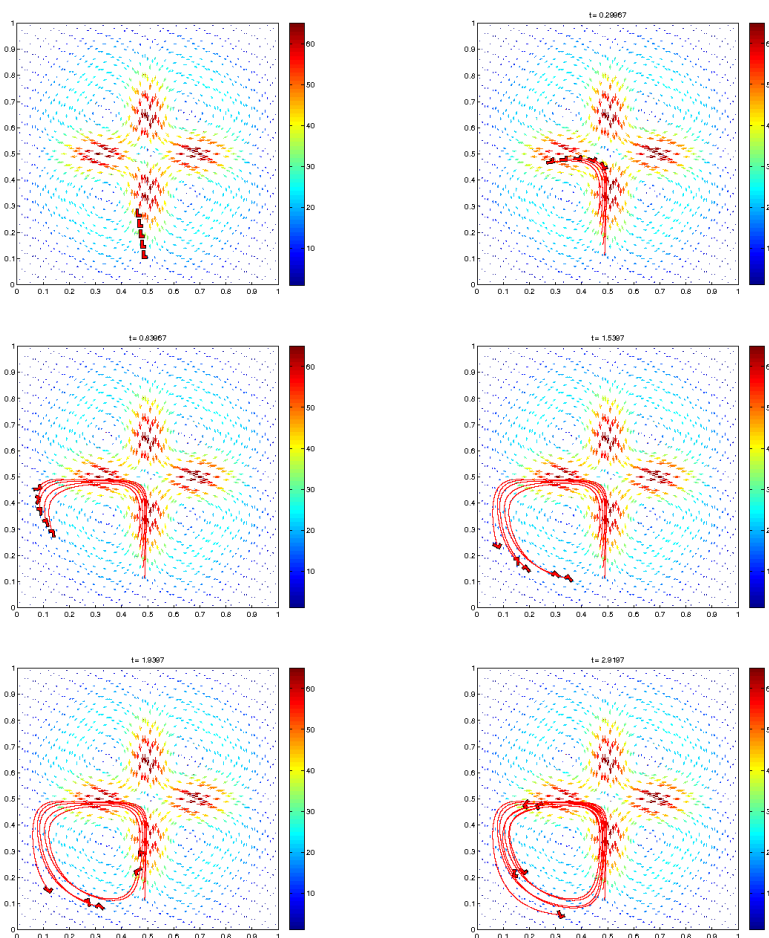


FIG. 4.4. Velocity field and motion of five right-handed L-shaped enantiomers initially placed in the middle between two counter-rotating vortices

- [7] K.A. Busch and M.A. Busch (eds.); *Chiral Analysis*. Elsevier, Amsterdam, 2006.
- [8] A.N. Collins, G. Sheldrake, and J. Crosby (eds.); *Chirality in Industry: The Commercial Manufacture and Applications of Optically Active Compounds*. Wiley, Chichester, 1995.
- [9] A.N. Collins, G. Sheldrake, and J. Crosby (eds.); *Chirality in Industry II: The Commercial Manufacture and Applications of Optically Active Compounds*. Wiley, Chichester, 1997.
- [10] E.U. Condon, W. Altar, and H. Eyring; *One electron rotatory power*. J. Chem. Phys. **5**, 479–491, 1937.
- [11] M. Eisenstein; *Cell sorting: divide and conquer*, Nature **441**, 1179–1185, 2006.
- [12] T. M. Fischer, M. Stohr-Liesen, and Schmid-Schönbein; Science **202**, 894, 1978.
- [13] E. Francotte and W. Lindner (eds.); *Chirality in Drug Research*. Wiley-VCH, Weinheim, 2006.
- [14] T. Franke, R.H.W. Hoppe, C. Linsenmann, L. Schmid, and C. Willbold; *Numerical*

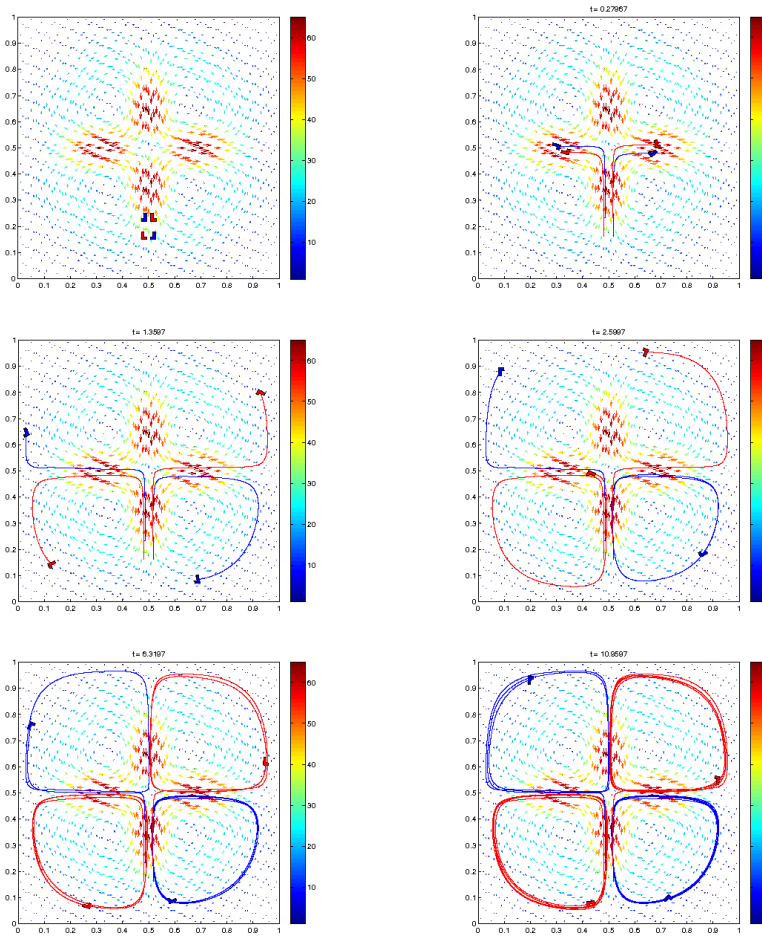


FIG. 4.5. Velocity field and motion of four L-shaped enantiomers (two left-handed and two-right-handed) initially placed in the middle between two counterrotating vortices

simulation of the motion and deformation of red blood cells and vesicles in microfluidic flows. *Comput. Visualiz. Sci.* **14**, 167-180, 2011.

- [15] J. Gal; *The discovery of biological enantioselectivity: Louis Pasteur and the fermentation of tartaric acid - a review and analysis 150 yr later.* *Chirality* **20**, 5–19, 2008.
- [16] A. Gantner, R.H.W. Hoppe, D. Köster, K.G. Siebert, and A. Wixforth; *Numerical simulation of piezoelectrically agitated surface acoustic waves on microfluidic biochips.* *Comp. Visual. Sci.* **10**, 145-161, 2007.
- [17] J.H. van 't Hoff; Utrecht, Netherlands, 1874.
- [18] R.H.W. Hoppe and C. Linsenmann; *An adaptive Newton continuation strategy for the fully implicit finite element immersed boundary method.* *J. Comp. Phys.* **231**, 4676–4693, 2012.
- [19] F. Hund; *Z. f. Phys.* **43**, 806, 1927.
- [20] D. Köster; *Numerical simulation of acoustic streaming on SAW-driven biochips.* *SIAM*

- J. Comp. Sci., **29**, 2352-2380, 2007.
- [21] M. Konrad; *Trennung chiraler Objekte in Mikroströmung*, Diploma Thesis, University of Augsburg, 2008.
- [22] M. Kostur, M. Schindler, P. Talkner, and P. Hänggi; *Chiral separation in microflows*. Phys. Rev. Lett. **96**, 014502-1 - 014502-4, 2006.
- [23] N. Kurihara and J. Miyamoto (eds.); *Chirality in Agrochemicals*. Wiley, Chichester, 1998.
- [24] J.A. LeBel; Bull. Soc. Chim. **22**, 337-347, 1874.
- [25] P.C.H. Li; *Microfluidic Lab-on-a-Chip for Chemical and Biological Analysis and Discovery*. CRC Press, Boca Raton, 2006.
- [26] Marcos, H.C. Fu, T.R. Powers, and R. Stocker; *Separation of microscale chiral objects by shear flow*. Phys. Rev. Lett. **102**, 158103-1 - 158103-4, 2009.
- [27] L. Pasteur; Compt. Rend. Acad. Sci. **26**, 535-538, 1848.
- [28] L. Pasteur; Compt. Rend. Acad. Sci. **37**, 110-114, 1853.
- [29] R.N. Patel (ed.); *Stereoselective Biocatalysis*. CRC Press, Boca Raton, 2000.
- [30] C. Peskin; *Numerical analysis of flood flow in the heart*. J. Comput. Phys. **25**, 220-252, 1977
- [31] C.S. Peskin; *The immersed boundary method*. Acta Numerica **11**, 479-517, 2002.
- [32] M. Quack and J. Strohner; *Parity violation in chiral molecules*. Chimia **59**, 530-538, 2005.
- [33] M. Quack, J. Strohner, and M. Willeke; *High-resolution spectroscopic studies and theory of parity violation in chiral molecules*. Ann. Rev. Phys. Chem. **59**, 741-769, 2008.
- [34] G.K.E.V. Scriba; *Cyclodextrins in capillary electrophoresis enantioseparations - Recent developments and applications*. J. Sep. Sci. **31**, 1991-2011, 2008.
- [35] P. Talkner, G. Ingold, and P. Hänggi; *Transport of flexible chiral objects in a uniform shear flow*. New Journal of Physics **14**, 073006, 2012.
- [36] L. Tartar; *Introduction to Sobolev Spaces and Interpolation Theory*. Springer, Berlin-Heidelberg-New York, 2007.
- [37] K. Tsubota, S. Wada, and T. Yamaguchi; *Simulation study on effects of hematocrit on blood flow properties using particle method*. J. Biomech. Sci. Eng. **1**, 159-170, 2006.
- [38] T. Wang, T.-W. Pan, Z.W. Xing, and R. Glowinski; *Numerical simulation of red blood cell rouleaus in microchannels*. Phys. Rev. E **79**, 041916-1 - 041916-11, 2009.
- [39] C.J. Welch; *Microscale chiral HPLC in support of pharmaceutical process research*. Chirality **21**, 114-118, 2009.
- [40] T. J. Wenzel; *Discrimination of Chiral Compounds using NMR Spectroscopy*. Wiley, Chichester, 2007.